Chemical Science

ROYAL SOCIETY OF CHEMISTRY

EDGE ARTICLE

View Article Online
View Journal | View Issue

Cite this: *Chem. Sci.*, 2025, **16**, 22127

All publication charges for this article have been paid for by the Royal Society of Chemistry

Rhodamine-functionalised rhodium(III) complexes: dual role as bioimaging agents and controllable reactive oxygen species photosensitisers for photocytotoxicity applications

Katherine Gui-Min Jiang, [ab] Fangfang Wei, [a] Peter Kam-Keung Leung, [bc] Siye Wu,[a] Kenneth Kam-Wing Lo *[bc] and Keith Man-Chung Wong *[a]

Received 15th July 2025
Accepted 7th October 2025

DOI: 10.1039/d5sc05257b

rsc.li/chemical-science

Compared to well-developed iridium(III) complexes, cyclometallated rhodium(III) complexes are underexplored as bioimaging reagents and photosensitisers, primarily due to the presence of non-emissive low-lying d–d excited states that limit their photophysical properties. In this work, a series of rhodamine-containing rhodium(III) complexes $[Rh(N^C)_2(bpy\text{-}Rho)](PF_6)_2$ was designed and synthesised to circumvent this problem. The incorporation of a rhodamine unit into cyclometallated rhodium(III) complexes endowed them with effective bioimaging and considerable reactive oxygen species (ROS) sensitisation capabilities upon low-energy photoexcitation. Time-resolved transient absorption spectroscopy of the complexes revealed a long-lived dark triplet state of rhodamine that was responsible for the enhanced ROS photosensitisation. An energy cascade pathway was proposed for the complexes, involving energy transfer from a rhodamine singlet excited state (S_1) to a $Rh(N^C)_2$-based triplet excited state (T_1'), and ultimately to the lowest-lying rhodamine-based triplet excited state (T_1). Through a judicious choice of cyclometallating ligands, the energy cascade efficiency can be modulated to achieve a delicate balance between fluorescence and ROS photosensitisation. Furthermore, the complexes specifically accumulated in the mitochondria and showed excellent photocytotoxicity by inducing pyroptosis, highlighting their potential as theranostic agents for bioimaging and photodynamic therapy.

Introduction

Photodynamic therapy (PDT) has gained prominence as a minimally invasive approach to cancer treatment, where a photosensitiser (PS) is activated by light irradiation, generating cytotoxic reactive oxygen species (ROS) to kill tumour cells.[1–3] In PDT, ROS are photogenerated in a spatiotemporally controlled manner at the tumour site, thereby reducing collateral damage to the surrounding healthy tissues. Typically, a PS is excited and finally populates the lowest-lying triplet state. In this state, it can (1) transfer electrons to nearby substrates, generating radicals such as hydroxyl radicals ($HO^{\bullet}$) and superoxide anion radicals ($O_2^{\bullet-}$) *via* the type I process; or (2) transfer energy to molecular oxygen ($^3O_2$) to produce highly cytotoxic singlet oxygen ($^1O_2$) through the type II process.[4,5] The generation of ROS *via* the type II photochemical reaction is mechanistically simpler than that *via* the type I process and is particularly effective under normoxic conditions.[6] In contrast, type I PDT is less dependent on oxygen, ensuring effective ROS generation even in hypoxic tumour microenvironments.[7] To maximise the therapeutic efficacy of PDT, the development of PSs that integrate both type I and type II photochemical processes represents a promising strategy.

Pyroptosis, a recently identified form of programmed cell death, is capable of triggering a strong immune stimulation response and has gained increasing attention.[8] However, it is predominantly induced by chemotherapeutic drugs, which may cause severe side effects.[9–11] With the development of PSs, it has been reported that pyroptosis can be induced by the ROS produced during PDT.[12–15] Given the short lifetimes (<40 ns) and narrow diffusion radii (*ca.* 10 nm) of ROS,[4] developing organelle-targeting PSs to achieve precise treatment is of paramount importance. Mitochondria are essential organelles involved in energy production and are recognised as crucial regulators of cell death.[16] Pyroptosis has also been closely linked to mitochondrial dysfunction.[17–20] Consequently, the development of mitochondria-targeting photosensitisers that can

[a]*Department of Chemistry, Southern University of Science and Technology, 1088 Xueyuan Boulevard, Shenzhen 518022, P. R. China. E-mail: keithwongmc@sustech.edu.cn*

[b]*Department of Chemistry, City University of Hong Kong, Tat Chee Avenue, Kowloon, Hong Kong, P. R. China. E-mail: bhkenlo@cityu.edu.hk*

[c]*State Key Laboratory of Terahertz and Millimetre Waves, City University of Hong Kong, Tat Chee Avenue, Kowloon, Hong Kong, P. R. China*

induce pyroptosis for cancer therapy presents a promising approach with excellent therapeutic performance.

Photofunctional transition metal complexes have attracted considerable attention as PSs due to their versatile photophysical and photochemical properties.[21–24] Among these complexes, cyclometallated iridium(III) complexes exhibit remarkable properties in PDT-based disease treatment, such as strong phosphorescence and efficient ROS photosensitisation.[25–28] As congeners of iridium(III) complexes, cyclometallated rhodium(III) complexes share similar synthetic methodologies and structural characteristics,[29] and they also possess unique advantages in therapeutic applications. Various rhodium(III) complexes have been reported to show significant anticancer activity through diverse mechanisms, such as inhibiting protein activity[30–32] or binding to DNA.[33–35] Furthermore, several mitochondria-targeting rhodium(III) complexes have been demonstrated as anticancer candidates, capable of disrupting the integrity of the mitochondrial membrane, elevating intracellular ROS levels, and inducing cell apoptosis.[36,37] These intriguing properties render rhodium(III) complexes potent therapeutic agents for different disease treatments. However, most cyclometallated rhodium(III) complexes possess a non-emissive low-lying d–d ligand-field excited state, which limits their applications in bioimaging and phototherapeutics. Only a few luminescent cyclometallated rhodium(III) complexes have been developed for cellular imaging,[29,38] and two dinuclear rhodium(II) complexes and one half-sandwich pentamethylcyclopentadienyl-rhodium(III) complex can photosensitise ROS for PDT applications.[39,40] Consequently, substantial challenges remain in utilising cyclometallated rhodium(III) complexes as potential bioimaging and phototherapeutic agents.

We have previously proposed a versatile strategy to synthesise a series of rhodamine-containing transition metal complexes, which integrates the merits of transition metal complexes and rhodamine dyes, such as efficient photoinduced generation of $^1O_2$ and high molar absorptivity in the visible region, respectively.[41] We have also demonstrated the improvement of $^1O_2$ generation quantum yields in rhodamine-containing iridium(III) complexes by strategically tuning the metal-based excited state (variation of the cyclometallating ligand) for subsequent energy transfer processes.[42,43] Inspired by the results of these studies, we anticipate that leveraging the energy cascade concept and the relatively weak spin–orbit coupling (SOC) characteristics of the rhodium atom, cyclometallated rhodium(III) complexes can be designed to achieve a delicate balance between fluorescence for bioimaging and ROS generation for PDT, highlighting their potential as phototherapeutic agents (Fig. 1). Herein, we report the design and synthesis of a series of rhodamine-containing cyclometallated rhodium(III) complexes with varied cyclometallating ligands, $[Rh(N^C)_2(bpy\text{-}Rho)](PF_6)_2$ (HN^C = 4-(2-pyridinyl)benzaldehyde (Hpba) (**1**), 2,3-diphenylquinoxaline (Hdpqx) (**2**), 2,3-dithienylquinoxaline (Hdtqx) (**3**), 2,3-diphenylbenzo[*g*]quinoxaline (Hdpbq) (**4**) and 2,3-dithienylbenzo[*g*]quinoxaline (Hdtbq) (**5**); bpy-Rho = 4-(9-(3,6-bis(diethylamino))xanthylium)-4′-methyl-2,2′-bipyridine), as bioimaging and phototherapeutic agents (Chart 1). Their rhodamine-free counterparts, $[Rh(N^C)_2(Me_2\text{-}bpy)](PF_6)$ (HN^C = Hpba (**1c**), Hdpqx (**2c**), Hdtqx (**3c**), Hdpbq (**4c**) and Hdtbq (**5c**); Me_2-bpy = 4,4′-dimethyl-2,2′-bipyridine), were also

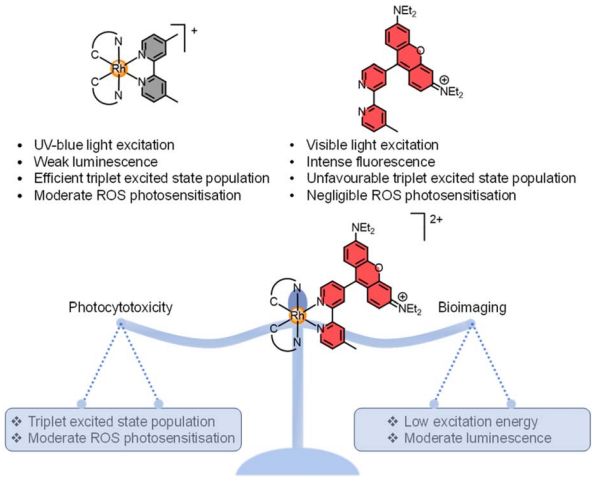

Fig. 1 Synergism of rhodamine-appended rhodium(III) complexes.

prepared for comparative studies. The incorporation of rhodamine into these rhodium(III) complexes enabled their excitation at relatively long wavelengths (>550 nm), yielding moderate emission quantum yields. Importantly, the $Rh(N^C)_2$-based triplet excited state (T_1') also functioned as a cascade, featuring another energy transfer pathway. Although intersystem crossing from the rhodamine singlet excited state (S_1) to its triplet excited state (T_1) is inefficient due to the weak SOC of the rhodium(III) centre, the new pathway facilitates the population of the rhodamine T_1 state, which is responsible for the photosensitisation of ROS. In contrast to previous iridium(III)–rhodamine systems,[41–44] the new rhodium(III)–rhodamine hybrid system maintains a delicate balance between fluorescence and ROS photosensitisation. Remarkably, their excellent photocytotoxicity towards MCF-7 cells *via* the introduction of pyroptosis unveils their great potential as PDT agents.

Results and discussion

Synthesis and characterisation

The rhodamine-appended rhodium(III) complexes **1–5** and their rhodamine-free counterparts (**1c–5c**) were synthesised according to modified procedures.[41] All the complexes were

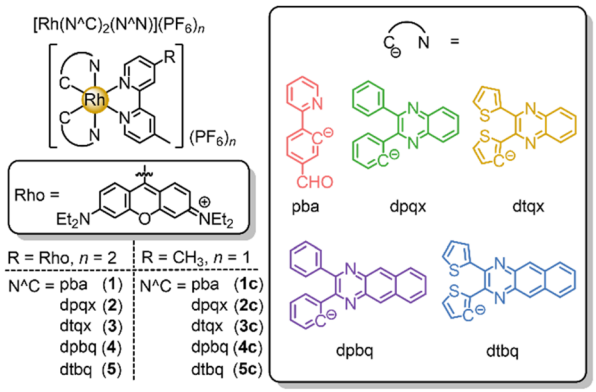

Chart 1 Structures of complexes **1–5** and **1c–5c**.

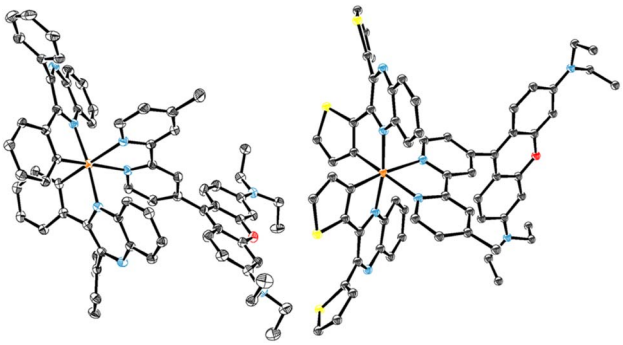

Fig. 2 Perspective views of complex cations of **2** (left) and **3** (right). Hydrogen atoms, counterions and solvent molecules are omitted for clarity. Thermal ellipsoids are shown at the 30% probability level. Rh: orange; S: yellow; N: blue; O: red; C: black.

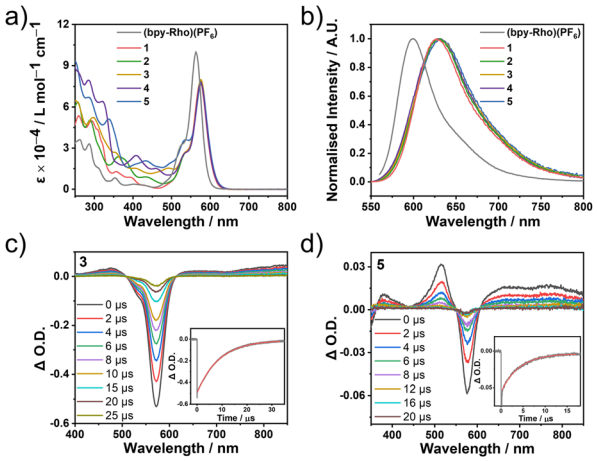

Fig. 3 (a) Electronic absorption and (b) normalised emission spectra of (bpy-Rho)(PF_6) and complexes **1**–**5** in aerated CH_3CN at 298 K (λ_{ex} = 525 nm). Nanosecond time-resolved transient absorption difference spectra of (c) complex **3** and (d) complex **5** in deaerated CH_3CN at 298 K (λ_{ex} = 532 nm). Insets in (c and d) show the decay traces of the signals at 575 nm.

characterised by ^{1}H and ^{13}C NMR and high-resolution electrospray ionisation mass spectrometry (HR-ESI-MS) and gave satisfactory elemental analyses (see the SI). The structures of complexes **2**, **3**, **4c** and **5c** were determined by X-ray crystallography. Their crystallographic data are listed in Table S1–S4 and their perspective views are depicted in Fig. 2 and S1. The complex cations exhibited distorted octahedral geometries, with *trans* angles at the rhodium(III) centre ranging from 169.5 to 175.6° for complex **2** and from 170.5 to 173.5° for complex **3**. As expected, the Rh–C bonds of the cyclometallating ligands were arranged in a *cis* orientation. In complex **2**, the dihedral angles between the bonded phenyl ring and the quinoxaline of the dpqx ligand were 24.5 and 24.3°, while those of the pendant phenyl ring were 49.7 and 50.6°. In complex **3**, the dihedral angles between the bonded thienyl ring and the quinoxaline of the dtqx ligand were 24.7 and 26.9°, and those of the pendant thienyl ring were 29.7 and 31.0°. The xanthene plane of the rhodamine unit was orthogonal to the pyridine plane, with dihedral angles of 63.6° in complex **2** and 74.2° in complex **3**.

Photophysical properties

The electronic absorption spectra of complexes **1**–**5** in CH_3CN at 298 K are presented in Table S5 and Fig. 3a. All the complexes exhibited moderately intense absorption bands at *ca.* 350–500 nm, which were ascribed to spin-allowed intraligand (^{1}IL) transitions ($\pi \rightarrow \pi^*$) or intraligand charge transfer (^{1}ILCT) [π(C-donor aryl of N^C) $\rightarrow$ π^*(N-donor aryl of N^C)], mixed with partial spin-allowed metal-to-ligand charge transfer (^{1}MLCT) [dπ(Rh) $\rightarrow$ π^*(N^C)] character.[45–47] An intense low-energy absorption band at *ca.* 575 nm was observed, which is assigned to the characteristic ^{1}IL ($\pi \rightarrow \pi^*$) transition of rhodamine.[41–43] It was absent in their rhodamine-free counterparts **1c**–**5c** (Fig. S2). Upon photoexcitation, all the rhodamine-containing complexes exhibited weak to moderate emission in fluid solutions at 298 K (Φ_{em} = 0.039–0.25; Table 1, Fig. 3b, and S3) with peak maxima at 605–631 nm. Compared to previously reported iridium(III)–rhodamine complexes (Φ_{em} = 0.003–0.037),[43] the emission quantum yields of complexes **1**–**5** were higher, making them promising bioimaging agents. Their emission intensities were insensitive to oxygen (Fig. S4 and S5), and their lifetimes were very short (<10 ns), suggesting that the emission was fluorescence in nature, attributed to the ^{1}IL excited state of rhodamine.[41–43] Notably, the emission maxima of the rhodamine complexes **1**–**5** were hypsochromically shifted in aqueous buffer solutions (Table 1), probably due to the hydrophobic nature of the cyclometallating ligands that promoted the aggregation of the complexes in aqueous media. When excited at 532 nm, no obvious phosphorescence from the Rh(N^C)$_2$-based moiety was observed, both in aerated and deaerated solutions (Fig. S4). However, upon 350-nm photoexcitation, complex **5** showed weak emission at *ca.* 750 nm in deaerated CH_3CN (Fig. S5), which is ascribed to the phosphorescence of the Rh(dtbq)$_2$-based moiety (*vide infra*). It is interesting to note that the absorption and emission bands of

Table 1 Photophysical data of the ligand (bpy-Rho)(PF_6) and complexes **1**–**5** at 298 K

Compound	Solvent	λ_{em}/nm	Φ_{em}[a]	τ_{TA}[b]/μs
(bpy-Rho)(PF_6)[41]	CH_3CN	598	0.29	—[c]
	Buffer[d]	598	0.23	
1	CH_3CN	627	0.22	20.0
	Buffer[d]	621	0.19	
2	CH_3CN	630	0.25	28.2
	Buffer[d]	625	0.19	
3	CH_3CN	630	0.072	8.7
	Buffer[d]	627	0.061	
4	CH_3CN	630	0.097	7.6
	Buffer[d]	605	0.081	
5	CH_3CN	631	0.064	4.1
	Buffer[d]	615	0.039	

[a] The absolute emission quantum yields were measured using an integrating sphere (λ_{ex} = 570 nm). [b] The TA lifetimes (τ_{TA}) at 575 nm (λ_{ex} = 532 nm) were examined in deaerated CH_3CN at 298 K. [c] Could not be determined. [d] Potassium phosphate buffer (50 mM, pH 7.4)/CH_3CN (7 : 3, v/v). The use of CH_3CN was due to solubility reasons.

rhodamine in complexes **1–5** are red-shifted relative to those in the free ligand (bpy-Rho)(PF_6) in CH_3CN (Table 1 and Fig. 3b), suggesting the effective coupling between the rhodium(III) centre and rhodamine moiety. Additionally, the Φ_{em} values of complexes **3–5** (0.064–0.097) were much lower than that of (bpy-Rho)(PF_6) (0.29) (Table 1), indicating the presence of a quenching process of the rhodamine S_1 state upon the incorporation of a rhodium(III) centre. In contrast, the rhodamine-free complexes **1c–5c** showed phosphorescence in the yellow to near-infrared (NIR) region (Table S6, Fig. S6 and S7), depending on the nature of the cyclometallating ligands.

Given the reduced emission quantum yields of complexes **1–5** compared to (bpy-Rho)(PF_6), a dark triplet excited state is anticipated to be populated as the lowest-lying excited state. The dark excited state of complexes **1–5** was examined by nanosecond time-resolved transient absorption (TA) spectroscopy, and the time-resolved TA spectra are depicted in Fig. 3c, d and S8. Upon 532-nm pulsed laser excitation, complexes **1–5** exhibited an intense and long-lived photobleaching signal at *ca.* 575 nm, originating from the ground-state rhodamine absorption depletion, which was assigned to the ^{3}IL excited state of rhodamine.[41–43] Based on the absence of such a TA signal in the free ligand (bpy-Rho)(PF_6),[41] the population of this rhodamine triplet excited state is attributed to the coordination of the ligand to the rhodium(III) centre. Complexes **1–5** displayed long triplet excited-state lifetimes on the microsecond timescale (4.1–28.2 μs) (Table 1). In the spectra of complex **5** (Fig. 3d), a positive peak was observed at *ca.* 516 nm with a lifetime of 3.8 μs. A similar signal was also observed in the TA spectra of complex **5c** (Fig. S9), and this positive TA peak was ascribed to the biscyclometallated rhodium(III) moiety-based ^{3}IL/^{3}MLCT excited state. Both the triplet excited-states on the rhodamine unit (^{3}IL) and the Rh(dtbq)$_2$-based moiety (^{3}IL/^{3}MLCT) were simultaneously populated in complex **5**, which was probably due to the existence of a thermal equilibrium between these closely-lying triplet excited states.[48,49]

ROS photosensitisation

To investigate the possible ROS photosensitisation capabilities of the rhodium(III) complexes, a fluorogenic probe for ROS, 2,7-dichlorofluorescein diacetate (DCFH-DA), was employed for a semi-quantitative study. In the presence of ROS, DCFH-DA is oxidised to the highly emissive 2,7-dichlorofluorescein (DCF).[50,51] Mixed solutions of (bpy-Rho)(PF_6) or rhodium(III) complexes and DCFH-DA were exposed to white-light irradiation (400–700 nm, 2 mW cm^{-2}), while the emission from DCF in the mixtures at 526 nm was monitored at 1-min intervals (Fig. 4a). As expected, negligible ROS was photogenerated by (bpy-Rho)(PF_6). Interestingly, the ROS photosensitising abilities of complexes **2–5** increased significantly, while that of complex **1** was still weak. Their total ROS generation abilities followed the order: (bpy-Rho)(PF_6) < **1** < **2** < **4** < **3** < **5**. By comparison with their rhodamine-free counterparts **1c–5c** (Fig. S10), the ROS generation abilities of complexes **1** and **2** were only slightly enhanced, while a significant increase in ROS generation was observed for complexes **3–5**. These results clearly demonstrate

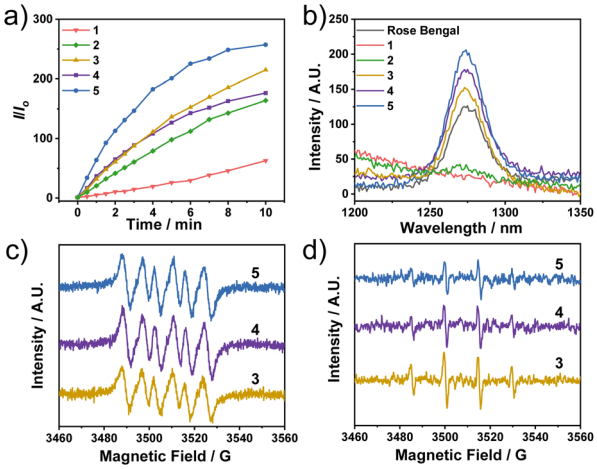

Fig. 4 (a) Emission enhancement of an aerated PBS solution of DCF (40 μM) and free ligand (bpy-Rho)(PF_6) or complexes **1–5** (0.5 μM) at 526 nm upon irradiation with white light (400–700 nm, 2 mW cm^{-2}). (b) $^1O_2$ emission spectra of complexes **1–5** and Rose Bengal in aerated CH_3CN (λ_{ex} = 573 nm). (c) EPR signals of DMPO–$O_2^{\bullet-}$ obtained upon white light irradiation (400–700 nm, 10 mW cm^{-2}) for 10 min of aerated MeOH solutions of complexes **3–5** (20 μM) and DMPO (100 mM). (d) EPR signals of DMPO–HO$^\bullet$ obtained upon white light irradiation (400–700 nm, 10 mW cm^{-2}) for 10 min of aerated PBS solutions of complexes **3–5** (20 μM) and DMPO (100 mM).

that the introduction of a rhodamine unit, as well as the choice of cyclometallating ligands, plays a vital role in the ROS generation efficiencies.

To identify the ROS produced by complexes **1–5**, various measurements were employed for the investigation of $^1O_2$, $O_2^{\bullet-}$ and HO$^\bullet$. First, the $^1O_2$ generation quantum yields of all complexes were determined by directly measuring the $^1O_2$ emission at *ca.* 1270 nm in aerated CH_3CN using Rose Bengal as a reference photosensitiser (Φ_Δ = 0.45 in CH_3CN).[52] As shown in Table 2 and Fig. 4b, very weak or negligible $^1O_2$ emission was detected for complexes **1** and **2**. Notably, a characteristic $^1O_2$ emission band was observed in the spectra of complexes **3–5**, and their $^1O_2$ generation efficiencies (Φ_Δ = 0.50 (**3**), 0.55 (**4**) and 0.75 (**5**)) were even higher than that of Rose Bengal. Additionally, similar results were obtained by monitoring the

Table 2 $^1O_2$ generation quantum yields of the ligand (bpy-Rho)(PF_6) and complexes **1–5** in aerated CH_3CN at 298 K

Compound	$\Phi_\Delta{}^a$	$\Phi_\Delta{}^b$
(bpy-Rho)(PF_6)[41]	0.002	—[c]
1	0.008	—[c]
2	0.11	—[c]
3	0.50	0.49
4	0.55	0.58
5	0.75	0.73

[a] The $^1O_2$ generation quantum yields were determined by using DPBF as a $^1O_2$ scavenger and Rose Bengal (Φ_Δ = 0.45 in aerated CH_3CN) was used as a reference (λ_{ex} = 570 nm). [b] The $^1O_2$ generation quantum yields were determined based on the emission of $^1O_2$ at 1270 nm (λ_{ex} = 570 nm). [c] Could not be determined.

diminution of 1,3-diphenylisobenzofuran (DPBF) absorbance at 410 nm (Table 2).

Considering the superior ROS generation efficiencies of complexes **3–5**, electron paramagnetic resonance (EPR) spectroscopy was employed to verify the generation of $O_2^{\bullet-}$ and HO$^\bullet$ by using 5,5-dimethyl-1-pyrroline-*N*-oxide (DMPO) as a spin-trapping agent. As shown in Fig. 4c, distinct DMPO–$O_2^{\bullet-}$ signals were observed in the presence of complexes **3–5**, suggestive of the $O_2^{\bullet-}$ production capacity of these complexes. Furthermore, a characteristic quartet signal of DMPO–HO$^\bullet$ with an intensity of 1 : 2 : 2 : 1, was detected in aqueous solutions containing complexes **3–5** upon light irradiation (Fig. 4d), revealing the formation of HO$^\bullet$ radicals. Thus, the efficient formation of ROS in these rhodamine-containing rhodium(III) complexes *via* both type I and type II mechanisms makes them highly promising candidates for PDT applications.

In general, the fluorescence and ROS photosensitisation properties of the rhodamine-containing rhodium(III) complexes are attributed to the rhodamine-based S_1 and T_1 states, respectively, offering two complementary decay pathways for the excited rhodamine-containing rhodium(III) complexes. The free ligand (bpy-Rho)(PF_6) showed intense fluorescence but negligible population of the triplet excited state and ROS photosensitisation. Complexes **1** and **2** exhibited high emission quantum yields (0.22 and 0.25, respectively; Table 1), which are comparable to that of (bpy-Rho)(PF_6) (0.29), suggesting that fluorescence was the predominant relaxation pathway. In light of the relatively low ROS generation efficiencies of complexes **1** and **2** (Φ_Δ = 0.008 and 0.11, respectively; Table 2), together with their relatively high emission quantum yields, an inefficient intersystem crossing (ISC) process for the population of the rhodamine-based T_1 state is anticipated due to the weak heavy atom effect of rhodium(III) with a relatively small SOC constant (ζ = *ca.* 1360 cm^{-1}).[53,54] However, in complexes **3–5**, the rhodamine fluorescence intensities decreased substantially (Φ_{em} = 0.064–0.097; Table 1), accompanied by high ROS (including $^1O_2$, $O_2^{\bullet-}$ and HO$^\bullet$) generation efficiencies. Given that the ISC rate in complexes **1–5** is mediated by the rhodium(III) centre and thus should be very similar among the five complexes, the population of the T_1 state in complexes **3–5** is enhanced by the variation of cyclometallating ligands, which are closely associated with the energy levels of Rh(N^C)$_2$-based T_1' states. Therefore, it is reasonable to assume that the rhodamine-based T_1 state can be independently populated from the rhodamine-based S_1 state through an additional energy transfer pathway. To elucidate the underlying energy transfer pathways, the energy levels of the S_1 and T_1 states in the rhodium(III)–rhodamine hybrid systems were estimated. The energy levels of S_1 and T_1 states of (bpy-Rho)(PF_6) were determined to be 2.14 and 1.70 eV,[41–43] respectively, while those of Rh(N^C)$_2$-based T_1' states were estimated from the emission spectra of the rhodamine-free analogues **1c–5c**, ranging from *ca.* 1.75 to 2.58 eV. This comparison indicates that the rhodamine T_1 state, as the lowest-lying excited state, is populated and primarily responsible for ROS photosensitisation.

An energy level diagram illustrating the excited-state dynamics of the rhodamine-decorated rhodium(III) complexes is shown in Fig. 5. Upon irradiation, complexes **1** and **2** are excited to the rhodamine S_1 state, and their rhodamine-based T_1 states are not readily accessible due to insufficient ISC efficiency. Although the Rh(N^C)$_2$-based T_1' states of complexes **1** and **2** could also contribute to ROS generation, the excitation energy at the absorption peak of rhodamine is lower than that required to access the ^{1}IL/^{1}MLCT state, which would further transfer energy to the T_1' state. For complexes **1** and **2**, the energy levels of the T_1' state (2.58 and 2.30 eV, respectively) are higher than that of the rhodamine S_1 state (2.14 eV), suggesting that the T_1' state cannot be populated from the S_1 state *via* an ISC process. For complexes **3–5**, the energy levels of the T_1' state (2.07–1.75 eV) lie between those of the rhodamine-based S_1 and T_1 states. The smaller energy gap between S_1 and T_1' states (ΔE_{S-T}) facilitates the ISC process.[43] Therefore, an energy cascade involving energy transfer from the rhodamine-based S_1 state to Rh(N^C)$_2$-based T_1' state *via* intramolecular singlet–triplet energy transfer (STET, $S_1 \rightarrow T_1'$), and further conveyed to the lowest-lying rhodamine-based T_1 state *via* a triplet–triplet energy transfer (TTET, $T_1' \rightarrow T_1$) process, is proposed.[55] As a result, the rhodamine-based long-lived non-emissive T_1 state is populated as the lowest-lying excited state, which is responsible for $^1O_2$ production *via* energy transfer to $^3O_2$ and for radical generation *via* electron transfer to substrates, respectively. Additionally, Förster resonance energy transfer (FRET) and photoinduced electron transfer (PET) were considered as potential mechanisms for the reduced rhodamine emission quantum yields of complexes **3–5**. However, given the minimal overlap between the fluorescence spectrum of rhodamine and the absorption spectra of rhodamine-free analogues, the theoretical quenching efficiencies (E_{calc}) of complexes **1–4** were determined to be 0.19–0.56 (Table S7), indicating that FRET alone is unlikely to account for the reduction of fluorescence intensities. In contrast, complex **5** displayed a long Förster distance (R_0) (22.58 Å), and the E_{calc} was estimated to be 0.99 (Table S7 and Fig. S11), suggesting that FRET contributes to its suppressed fluorescence. Based on the electrochemical data of the ligand (bpy-Rho)(PF_6) and rhodamine-free complexes **1c–5c** (Table S8), the driving force for PET from the rhodamine unit to the biscyclometallated rhodium(III) moiety was estimated using the equation for the "Gibbs energy of PET" (ΔG_{ET}). The ΔG_{ET} values of complexes **1–3** were calculated to be 0.12–0.51 eV, suggesting that PET is thermodynamically unfavourable in these complexes. The

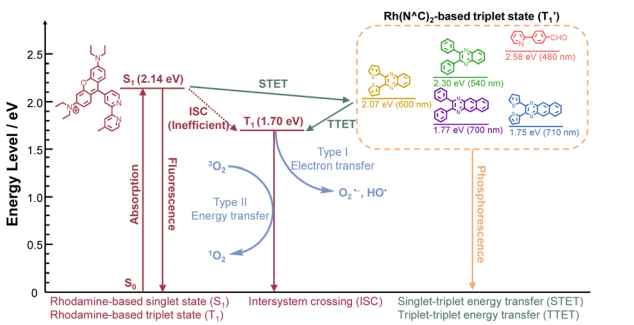

Fig. 5 Energy level diagram of rhodamine-decorated rhodium(III) complexes.

ΔG_{ET} values of complexes **4** and **5** were determined to be −0.04 and −0.07 eV, respectively. However, the values are quite small, suggesting that the quenching of rhodamine fluorescence is not attributable to PET. These results highlight that the ROS generation properties of rhodamine-decorated rhodium(III) complexes can be controlled through a judicious selection of cyclometallating ligands in this hybrid system.

Bioimaging and (photo)cytotoxicity

The biological properties of complexes **1–5** were studied using human breast carcinoma MCF-7 cells as a model cancer cell line. The intracellular localisation of the complexes was investigated by laser-scanning confocal microscopy (LSCM). After treatment of MCF-7 cells with complexes **1–5**, intense emission was observed in the cytoplasmic region of the cells (Fig. 6a and S12), indicating the highly efficient cellular uptake of these complexes. The reticulum-like network observed appeared to be mitochondria. Colocalisation studies demonstrated that these complexes accumulated in the mitochondria of live cells with relatively high Pearson's correlation coefficients (PCCs; 0.80–0.89) (Fig. 6a, S12 and S13). Their exclusive mitochondria-targeting abilities are attributed to their cationic and lipophilic character ($\log D_{7.4}$ ranging from +1.06 to +0.19, Table S9).[56–59] As revealed by inductively coupled plasma-mass spectrometry (ICP-MS), the relatively lower cellular uptake of complexes **4** and **5** ([Rh] = 0.049 and 0.039 fmol, respectively; Table S10) compared to that of the other three complexes ([Rh] = 0.061–0.097 fmol; Table S10) can be attributed to their larger molecular sizes, resulting from the cyclometallating ligands.

To evaluate the PDT performance of these rhodamine-decorated rhodium(III) complexes, their (photo)cytotoxicity towards MCF-7 cells was studied using the 3-(4,5-dimethylthiazol-2-yl)-2,5-diphenyltetrazolium bromide (MTT) assay. All the complexes exhibited minimal cytotoxicity in the dark with $IC_{50,dark}$ values > 50 μM (Table 3 and Fig. S14). Upon white-light irradiation (400–700 nm, 10 mW cm^{-2}, 30 min), the cell viability decreased dramatically, and the complexes showed dose-dependent photocytotoxicity with $IC_{50,light}$ values at the sub-micromolar levels. Notably, complex **3** displayed the highest photocytotoxicity index ($IC_{50,dark}/IC_{50,light}$ > 313), which may be attributed to its relatively high cellular uptake efficiency (Table S10). It has been reported that HO$^{\bullet}$ is the most cytotoxic and reactive ROS in biological environments.[60] Since complex **3** showed the highest photocytotoxicity, it was further investigated using the Calcein-AM/propidium iodide (PI) staining assay. As presented in Fig. 6b, without light irradiation, complex **3**-treated MCF-7 cells displayed strong green fluorescence from Calcein-AM and no red emission from PI, indicating negligible cytotoxicity of complex **3** in the dark. Upon 525 nm irradiation (10 mW cm^{-2}), most cells were dead, as evidenced by the strong red fluorescence of PI. Quantification of the Calcein-AM/PI-stained cells by flow cytometry indicates that the live cell population in complex **3**-treated cells dropped significantly from *ca.* 99.10 to 0.62% upon photoirradiation (Fig. S15), suggesting the high photocytotoxicity of complex **3** and its great potential for PDT.

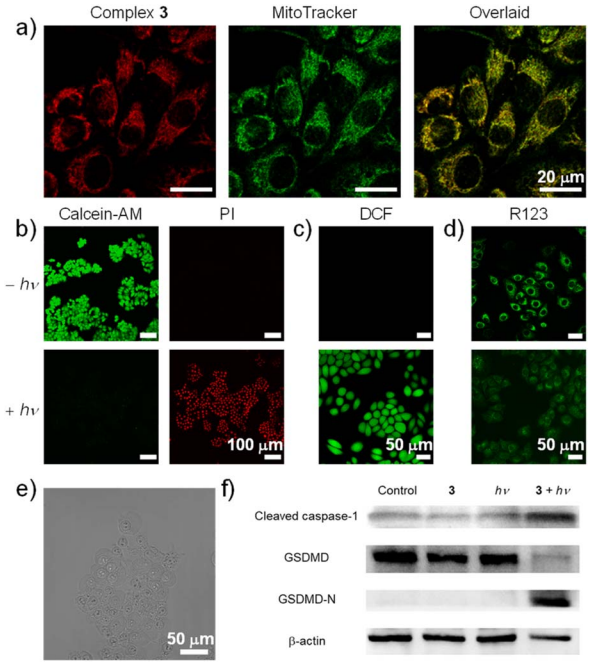

Fig. 6 (a) LSCM images of MCF-7 cells incubated with complex **3** (2 μM; λ_{ex} = 561 nm and λ_{em} = 575–650 nm) for 30 min, followed by staining with MitoTracker Green (200 nM; λ_{ex} = 488 nm and λ_{em} = 500–530 nm) for 15 min. PCC = 0.89. (b) Live/dead cell staining of MCF-7 cells incubated with complex **3** (2 μM) for 2 h, followed by either keeping in the dark or irradiation at 525 nm (10 mW cm^{-2}) for 10 min, and subsequently incubated for 1 h. Cells were stained with Calcein-AM (1 μM; λ_{ex} = 488 nm and λ_{em} = 500–520 nm) and PI (10 μM; λ_{ex} = 532 nm and λ_{em} = 600–650 nm) for 1 h. (c) Intracellular ROS generation in MCF-7 cells incubated with complex **3** (2 μM) for 2 h, followed by DCFH-DA (5 μM; λ_{ex} = 488 nm and λ_{em} = 500–530 nm) for 30 min and then kept in the dark or irradiated with white light (400–700 nm, 10 mW cm^{-2}) for 2 min. (d) Changes of MMP in MCF-7 cells incubated with complex **3** (2 μM) for 2 h and then kept in the dark or irradiated with white light (400–700 nm, 10 mW cm^{-2}) for 10 min. Cells were further incubated in the dark for 30 min before being stained with R123 (5 μM; λ_{ex} = 488 nm and λ_{em} = 500–530 nm) for 10 min. (e) A bright-field LSCM image of MCF-7 cells incubated with complex **3** (2 μM) for 2 h and then irradiated with white light (400–700 nm, 10 mW cm^{-2}) for 10 min. (f) Western blot analysis of cleaved caspase-1, GSDMD, GSDMD-N and β-actin in MCF-7 cells treated with or without complex **3** (1 μM) for 2 h in the presence or absence of 525 nm irradiation (10 mW cm^{-2}) for 5 min.

The intracellular ROS generation ability of complex **3** was examined using the ROS probe DCFH-DA. As expected, dramatically enhanced fluorescence of DCF was detected in the

Table 3 (Photo)cytotoxicity of complexes **1–5** towards MCF-7 cells in the dark and upon white-light irradiation (400–700 nm, 10 mW cm^{-2}) for 30 min. Photocytotoxicity index = $IC_{50,dark}/IC_{50,light}$

Complex	$IC_{50,dark}$/μM	$IC_{50,light}$/μM	Photocytotoxicity index
1	>100	4.7 ± 0.2	>21
2	>50	0.55 ± 0.02	>91
3	>50	0.16 ± 0.01	>313
4	>50	0.50 ± 0.01	>100
5	>50	0.39 ± 0.02	>128

cells only after white-light irradiation (400–700 nm, 10 mW cm^{-2}, 2 min) (Fig. 6c), indicating substantial ROS photosensitisation. When the cells were pretreated with NaN_3, Tiron or D-mannitol ($^1O_2$, $O_2^{\bullet-}$ and $HO^{\bullet}$ scavengers, respectively), the fluorescence intensity of DCF in MCF-7 cells decreased markedly (Fig. S16 and S17), implying the generation of ROS *via* type I and type II pathways in live cells. Considering the subcellular location of these rhodium(III) complexes, the mitochondrial membrane potential (MMP) of cells treated with complex **3** was measured utilising rhodamine 123 (R123) as an indicator. At higher potentials in living cells, R123 accumulates in mitochondria and emits strong green fluorescence. However, it is released from mitochondria at low MMP, resulting in weak emission. As shown in Fig. 6d, for MCF-7 cells treated with complex **3** in the dark, R123 accumulated in mitochondria, as indicated by intense green fluorescence. Upon photoirradiation, the intensity of green emission was dramatically reduced, illustrating the release of R123 and the loss of MMP. These results demonstrate that the ROS photosensitised by complex **3** can trigger mitochondrial damage and lead to cell death. The excellent therapeutic effects of these rhodamine–decorated rhodium(III) complexes were therefore attributed to their highly efficient ROS generation and mitochondria-targeting abilities.

Intriguingly, upon treatment with complex **3** and subsequent white light irradiation (400–700 nm, 10 mW cm^{-2}, 10 min), MCF-7 cells exhibited swelling and expulsion of large bubbles from the plasma membrane (Fig. 6e). These morphological changes indicated that complex **3** may trigger cell death *via* pyroptosis. A canonical initiating pathway of pyroptosis has been reported in which intracellular ROS activates NOD-like receptor protein 3 (NLRP3) inflammasomes, leading to the cleavage of pro-caspase-1, followed by the cleavage of gasdermin D (GSDMD).[61–64] The cleaved N-terminal domain of GSDMD (GSDMD-N) then translocates to the cell membrane, where it forms pores, resulting in cell swelling and membrane rupture.[65,66] Western blot assays were conducted to study the expression of cleaved caspase-1, GSDMD and GSDMD-N in MCF-7 cells under different conditions. Compared to untreated cells (control), cells treated with either light irradiation or complex **3** alone showed no significant variation in the expression levels of these proteins (Fig. 6f). However, cells treated with both complex **3** and light irradiation displayed a marked increase in cleaved caspase-1 expression, accompanied by a notable reduction in the GSDMD level and a corresponding elevation in the GSDMD-N level. It is likely that the activation of caspase-1 led to the cleavage of GSDMD into the GSDMD-N domain, ultimately triggering pyroptosis. Collectively, these findings suggest that upon photoexcitation, complex **3** can efficiently induce pyroptosis *via* a caspase-1-mediated GSDMD cleavage pathway.

Conclusion

In conclusion, we have developed a series of novel rhodamine-decorated rhodium(III) complexes that can function as both bioimaging and PDT agents. The incorporation of the rhodamine unit addresses some of the limitations associated with the use of cyclometallated rhodium(III) complexes in PDT. A long-lived dark rhodamine-based triplet state, resulting from the addition of the rhodium(III) centre, is the lowest-lying excited state and is responsible for ROS photosensitisation. Complexes **3–5** exhibited substantially enhanced $^1O_2$ generation efficiencies with low excitation energy at 570 nm. Meanwhile, they were capable of generating $O_2^{\bullet-}$ and $HO^{\bullet}$ efficiently. Based on photophysical and photochemical studies, we propose an energy cascade pathway from a rhodamine-based S_1 state to a $Rh(N^C)_2$-based T_1' state, and subsequently to the lowest rhodamine T_1 state when the energy level of the T_1' state lies in-between that of the S_1 and T_1 states of rhodamine. This discovery allows for modulating the ROS photosensitisation capability of cyclometallated rhodium(III) complexes through a judicious selection of cyclometallating ligands, maintaining a delicate balance between fluorescence and ROS photosensitisation within this system. Additionally, cellular studies revealed that these complexes were localised in mitochondria, and the photogenerated ROS triggered mitochondrial dysfunction. Furthermore, complex **3** was capable of inducing pyroptosis upon light irradiation, achieving excellent therapeutic effects by integrating type I and type II ROS photosensitisation processes. This work introduces a promising strategy for the development of cyclometallated rhodium(III) complexes as effective PSs. This rhodium(III)–rhodamine hybrid system is anticipated to function as an innovative theranostic agent for both imaging and PDT applications.

Author contributions

K. G.-M. J.: conceptualisation, data curation, formal analysis, investigation, writing – original draft, writing – review & editing; F. W.: conceptualisation, data curation; P. K.-K. L.: data curation, formal analysis, writing – original draft; S. W.: data curation; K. K.-W. L.: conceptualisation, funding acquisition, project administration, resources, supervision, writing – review & editing; K. M.-C. W.: conceptualisation, funding acquisition, project administration, resources, supervision, writing – review & editing.

Conflicts of interest

The authors declare no conflict of interest.

Data availability

Data are available in the supplementary information (SI). Supplementary information: instrumentation, methods, synthetic details, characterisation, analytical and photophysical data and results of cellular studies, microscopy experiments and bioassays. See DOI: **https://doi.org/10.1039/d5sc05257b**.

CCDC 2350904 (**2**), 2350905 (**3**), 2421313 (**4c**) and 2421314 (**5c**) contain the supplementary crystallographic data for this paper.[67a–d]

Acknowledgements

We thank the Hong Kong Research Grants Council (Project No. CityU 11309423 and CityU 11304524), the Hong Kong Research Grants Council and the Natural Science Foundation of China (Project No. N_CityU104/21), the National Natural Science Foundation of China (Grant No. 21771099), and the Science, Technology and Innovation Commission of Shenzhen Municipality (Grant No. JCYJ20190809165411528) for financial support. We also acknowledge the funding support from the "Laboratory for Synthetic Chemistry and Chemical Biology" under the Health@InnoHK Programme launched by the Innovation and Technology Commission, the Government of Hong Kong SAR, P. R. China. We are also grateful to Dr Jie Wang for his help in the biological studies. K. G.-M. J. acknowledges receipt of a Postgraduate Studentship administered by the Southern University of Science and Technology and City University of Hong Kong.

References

1 D. E. J. G. J. Dolmans, D. Fukumura and R. K. Jain, *Nat. Rev. Cancer*, 2003, **3**, 380.
2 S. Monro, K. L. Colón, H. Yin, J. Roque III, P. Konda, S. Gujar, R. P. Thummel, L. Lilge, C. G. Cameron and S. A. McFarland, *Chem. Rev.*, 2018, **119**, 797.
3 R. Weijer, M. Broekgaarden, M. Kos, R. van Vught, E. A. J. Rauws, E. Breukink, T. M. van Gulik, G. Storm and M. Heger, *J. Photochem. Photobiol., C*, 2015, **23**, 103.
4 T. C. Pham, V.-N. Nguyen, Y. Choi, S. Lee and J. Yoon, *Chem. Rev.*, 2021, **121**, 13454.
5 D. Chen, Q. Xu, W. Wang, J. Shao, W. Huang and X. Chen, *Small*, 2021, **17**, 2006742.
6 H. Abrahamse and M. R. Hamblin, *Biochem. J.*, 2016, **473**, 347.
7 T. Huang, H. Ji, S. Yan, Y. Zou, J. Li, J. W. Y. Lam, C. Han and B. Z. Tang, *Biomaterials*, 2023, **297**, 122108.
8 J. Shi, W. Gao and F. Shao, *Trends Biochem. Sci.*, 2017, **42**, 245.
9 Y. Wang, W. Gao, X. Shi, J. Ding, W. Liu, H. He, K. Wang and F. Shao, *Nature*, 2017, **547**, 99.
10 L. Li, S. Wang and W. Zhu, *Cancer*, 2023, **15**, 26.
11 L. Hu, M. Chen, X. Chen, C. Zhao, Z. Fang, H. Wang and H. Dai, *Cell Death Dis.*, 2020, **11**, 281.
12 F. Du, H. Zhao, Y. Song, Z. Feng, K. Liu, Z. Wang, R. Guo, L. Qiu, Q. Chen and L. Zhou, *Adv. Funct. Mater.*, 2024, **34**, 2406150.
13 S. Zeng, Y. Wang, C. Chen, H. Kim, X. Liu, M. Jiang, Y. Yu, Y. S. Kafuti, Q. Chen, J. Wang, X. Peng, H. Li and J. Yoon, *Angew. Chem., Int. Ed.*, 2024, **63**, e202316487.
14 Y. Lu, F. Xu, Y. Wang, C. Shi, Y. Sha, G. He, Q. Yao, K. Shao, W. Sun, J. Du, J. Fan and X. Peng, *Biomaterials*, 2021, **278**, 121167.
15 X. Su, W.-J. Wang, Q. Cao, H. Zhang, B. Liu, Y. Ling, X. Zhou and Z.-W. Mao, *Angew. Chem., Int. Ed.*, 2022, **61**, e202115800.
16 D. C. Wallace, *Nat. Rev. Cancer*, 2012, **12**, 685.
17 Y. Xiao, T. Zhang, X. Ma, Q.-C. Yang, L.-L. Yang, S.-C. Yang, M. Liang, Z. Xu and Z.-J. Sun, *Adv. Sci.*, 2021, **8**, 2101840.
18 B. Wang, H. Zhou, L. Chen, Y. Ding, X. Zhang, H. Chen, H. Liu, P. Li, Y. Chen, C. Yin and Q. Fan, *Angew. Chem., Int. Ed.*, 2024, **63**, e202308874.
19 X. Su, B. Liu, W.-J. Wang, K. Peng, B.-B. Liang, Y. Zheng, Q. Cao and Z.-W. Mao, *Angew. Chem., Int. Ed.*, 2023, **62**, e202216917.
20 J. Zhuang, Z. Ma, N. Li, H. Chen, L. Yang, Y. Lu, K. Guo, N. Zhao and B. Z. Tang, *Adv. Mater.*, 2024, **36**, 2309488.
21 L. C.-C. Lee and K. K.-W. Lo, *J. Am. Chem. Soc.*, 2022, **144**, 14420.
22 L. C.-C. Lee and K. K.-W. Lo, *Small Methods*, 2024, **8**, 2400563.
23 J. Li and T. Chen, *Coord. Chem. Rev.*, 2020, **418**, 213355.
24 L. K. McKenzie, H. E. Bryant and J. A. Weinstein, *Coord. Chem. Rev.*, 2019, **379**, 2.
25 J.-H. Zhu, G.-X. Xu, J. Shum, L. C.-C. Lee and K. K.-W. Lo, *Chem. Commun.*, 2021, **57**, 12008.
26 A. M.-H. Yip, C. K.-H. Lai, K. S.-M. Yiu and K. K.-W. Lo, *Angew. Chem., Int. Ed.*, 2022, **61**, e202116078.
27 L. Ke, F. Wei, L. Xie, J. Karges, Y. Chen, L. Ji and H. Ciao, *Angew. Chem., Int. Ed.*, 2022, **61**, e202205429.
28 J. Zhao, K. Yan, G. Xu, X. Liu, Q. Zhao, C. Xu and S. Gou, *Adv. Funct. Mater.*, 2022, **31**, 2008325.
29 S.-K. Leung, K. Y. Kwok, K. Y. Zhang and K. K.-W. Lo, *Inorg. Chem.*, 2010, **49**, 4984.
30 D.-L. Ma, L.-J. Liu, K.-H. Leung, Y.-T. Chen, H.-J. Zhong, D. S.-H. Chan, H.-M. D. Wang and C.-H. Leung, *Angew. Chem., Int. Ed.*, 2014, **53**, 9178.
31 G.-J. Yang, W. Wang, S. W. F. Mok, C. Wu, B. Y. K. Law, X.-M. Miao, K.-J. Wu, H.-J. Zhong, C.-Y. Wong, V. K. W. Wong, D.-L. Ma and C.-H. Leung, *Angew. Chem., Int. Ed.*, 2018, **57**, 13091.
32 G.-J. Yang, H.-J. Zhong, C.-N. Ko, S.-Y. Wong, K. Vellaisamy, M. Ye, D.-L. Ma and C.-H. Leung, *Chem. Commun.*, 2018, **54**, 2463.
33 K. M. Boyle and J. K. Barton, *J. Am. Chem. Soc.*, 2018, **140**, 5612.
34 A. Nano, J. Dai, J. M. Bailis and J. K. Barton, *Biochemistry*, 2021, **60**, 2055.
35 Y. Zheng, X.-X. Chen, D.-Y. Zhang, W.-J. Wang, K. Peng, Z.-Y. Li, Z.-W. Mao and C.-P. Tan, *Chem. Sci.*, 2023, **14**, 6890.
36 Y.-B. Peng, W. He, Q. Niu, C. Tao, X.-L. Zhong, C.-P. Tan and P. Zhao, *Dalton Trans.*, 2021, **50**, 9068.
37 Y.-B. Peng, C. Tao, C.-P. Tan and P. Zhao, *J. Inorg. Biochem.*, 2021, **218**, 111400.
38 M. Sohrabi, M. B. Torbati, M. Lutz, S. Meghdadi, H. Farrokhpour, A. Amiri and M. Amirnasr, *Chem. Commun.*, 2019, **55**, 2676.
39 L. E. Joyce, J. D. Aguirre, A. M. Angeles-Boza, A. Chouai, P. K.-L. Fu, K. R. Dunbar and C. Turro, *Inorg. Chem.*, 2010, **49**, 5371.
40 B. Zhang, J. Xiao, X. Wang, P. Li and W. Su, *Photodiagn. Photodyn. Ther.*, 2020, **32**, 102049.
41 C. Liu, L. Zhou, F. Wei, L. Li, S. Zhao, P. Gong, L. Cai and K. M.-C. Wong, *ACS Appl. Mater. Interfaces*, 2019, **11**, 8797.

42 L. Zhou, F. Wei, J. Xiang, H. Li, C. Li, P. Zhang, C. Liu, P. Gong, L. Cai and K. M.-C. Wong, *Chem. Sci.*, 2020, **11**, 12212.
43 F. Wei, F. Chen, S. Wu, M. Zha, J. Liu, K.-L. Wong, K. Li and K. M.-C. Wong, *Inorg. Chem.*, 2024, **63**, 5872.
44 J. Liu, X. Yang, S. Wu, P. Gong, F. Pan, P. Zhang, C.-S. Lee, C. Liu and K. M.-C. Wong, *J. Mater. Chem. B*, 2024, **12**, 3710.
45 F. Wei, S.-L. Lai, S. Zhao, M. Ng, M.-Y. Chan, V. W.-W. Yam and K. M.-C. Wong, *J. Am. Chem. Soc.*, 2019, **141**, 12863.
46 K. K.-W. Lo, C.-K. Li, K.-W. Lau and N. Zhu, *Dalton Trans.*, 2003, **2**, 4682.
47 J. Lu, S. Zhao, F. Wei and K. M.-C. Wong, *Eur. J. Inorg. Chem.*, 2023, **26**, e202200792.
48 S. Cerfontaine, L. Troian-Gautier, Q. Duez, J. Cornil, P. Gerbaux and B. Elias, *Inorg. Chem.*, 2021, **60**, 366.
49 A. Harriman, A. Khatyr and R. Ziessel, *Dalton Trans.*, 2003, 2061.
50 K.-i. Setsukinai, Y. Urano, K. Kakinuma, H. J. Majima and T. Nagano, *J. Biol. Chem.*, 2003, **278**, 3170.
51 Z. Lv, L. Zou, H. Wei, S. Liu, W. Huang and Q. Zhao, *ACS Appl. Mater. Interfaces*, 2018, **10**, 19523.
52 R. W. Redmond and J. N. Gamlin, *Photochem. Photobiol.*, 1999, **70**, 391.
53 M. Blume, *Phys. Rev.*, 1964, **134**, A320.
54 T. M. Dunn, *Trans. Faraday Soc.*, 1961, **57**, 48.
55 Y. Li, M. E. Köse and K. S. Schanze, *J. Phys. Chem. B*, 2013, **117**, 9025.
56 W. H.-T. Law, L. C.-C. Lee, M.-W. Louie, H.-W. Liu, T. W.-H. Ang and K. K.-W. Lo, *Inorg. Chem.*, 2013, **52**, 13029.
57 S. P.-Y. Li, C. T.-S. Lau, M.-W. Louie, Y.-W. Lam, S. H. Cheng and K. K.-W. Lo, *Biomaterials*, 2013, **34**, 7519.
58 S. P.-Y. Li, T. S.-M. Tang, K. S.-M. Yiu and K. K.-W. Lo, *Chem.–Eur. J.*, 2012, **18**, 13342.
59 B. Wang, Y. Liang, H. Dong, T. Tan, B. Zhan, J. Cheng, K. K.-W. Lo, Y. W. Lam and S. H. Cheng, *ChemBioChem*, 2012, **13**, 2729.
60 K.-X. Teng, L.-Y. Niu and Q.-Z. Yang, *J. Am. Chem. Soc.*, 2023, **145**, 4081.
61 Y. Fang, S. Tian, Y. Pan, W. Li, Q. Wang, Y. Tang, T. Yu, X. Wu, Y. Shi, P. Ma and Y. Shu, *Biomed. Pharmacother.*, 2020, **121**, 109595.
62 D. Zheng, J. Liu, H. Piao, Z. Zhu, R. Wei and K. Liu, *Front. Immunol.*, 2022, **13**, 1039241.
63 P. Yu, X. Zhang, N. Liu, L. Tang, C. Peng and X. Chen, *Signal Transduction Targeted Ther.*, 2021, **6**, 128.
64 K. Peng, Y. Zhang, W. Xia and Z.-W. Mao, *Chem. Soc. Rev.*, 2023, **52**, 2790.
65 M. Wu, X. Liu, H. Chen, Y. Duan, J. Liu, Y. Pan and B. Liu, *Angew. Chem., Int. Ed.*, 2021, **60**, 9093.
66 W. Zhang, Z. Liu, J. Zhu, Z. Liu, Y. Zhang, G. Qin, J. Ren and X. Qu, *J. Am. Chem. Soc.*, 2023, **145**, 16658.
67 (*a*) CCDC 2350904: Experimental Crystal Structure Determination, 2025, DOI: **10.5517/ccdc.csd.cc2jx9md**; (*b*) CCDC 2350905: Experimental Crystal Structure Determination, 2025, DOI: **10.5517/ccdc.csd.cc2jx9nf**; (*c*) CCDC 2421313: Experimental Crystal Structure Determination, 2025, DOI: **10.5517/ccdc.csd.cc2m8kwc**; (*d*) CCDC 2421314: Experimental Crystal Structure Determination, 2025, DOI: **10.5517/ccdc.csd.cc2m8kxd**.